Material-specific analysis using coherent-scatter imaging

Deidre L. Batchelar
Imaging Research Laboratories, The John P. Robarts Research Institute, London, Ontario N6A 5K8, Canada, and the Department of Medical Biophysics, The University of Western Ontario, London, Ontario N6A 5C1, Canada

Ian A. Cunningham[a)]
Imaging Research Laboratories, The John P. Robarts Research Institute, London, Ontario N6A 5K8, Canada, the Department of Medical Biophysics, The University of Western Ontario, London, Ontario N6A 5C1, Canada, and the Department of Diagnostic Radiology, London Health Sciences Centre, London, Ontario N6A 4G5, Canada

Coherent-scatter computed tomography (CSCT) is a novel imaging method we are developing to produce cross-sectional images based on the low-angle ($<10°$) scatter properties of tissue. At diagnostic energies, this scatter is primarily coherent with properties dependent upon the molecular structure of the scatterer. This facilitates the production of material-specific maps of each component in a conglomerate. Our particular goal is to obtain quantitative maps of bone-mineral content. A diagnostic x-ray source and image intensifier are used to acquire scatter patterns under first-generation CT geometry. An accurate measurement of the scatter patterns is necessary to correctly identify and quantify tissue composition. This requires corrections for exposure fluctuations, temporal lag in the intensifier, and self-attenuation within the specimen. The effect of lag is corrected using an approximate convolution method. Self-attenuation causes a cupping artifact in the CSCT images and is corrected using measurements of the transmitted primary beam. An accurate correction is required for reliable density measurements from material-specific images. The correction is shown to introduce negligible noise to the images and a theoretical expression for CSCT image SNR is confirmed by experiment. With these corrections, the scatter intensity is proportional to the number of scattering centers interrogated and quantitative measurements of each material (in g/cm^3) are obtained. Results are demonstrated using both a series of poly(methyl methacrylate) (PMMA) sheets of increasing thickness (2–12 mm) and a series of 5 acrylic rods containing varying amounts of hydroxyapatite (0–0.400 g/cm^3), simulating the physiological range of bone-mineral density (BMD) found in trabecular bone. The excellent agreement between known and measured BMD demonstrates the viability of CSCT as a tool for densitometry. © *2002 American Association of Physicists in Medicine.* [DOI: 10.1118/1.1493216]

Key words: coherent scatter, x-ray diffraction, computed tomography, tissue composition, bone-mineral density (BMD)

I. INTRODUCTION

Disease frequently impairs tissue function by altering its structure. This may occur at the cellular level, which may affect intramolecular configurations, or as gross tissue changes, such as the increased fat content of trabecular bone in osteoporosis. An imaging technique responsive to changes at the molecular level may, therefore, provide a sensitive means of distinguishing diseased and normal tissue. Coherent-scatter-based imaging provides such a modality. Coherent scatter is a generalization of Thomson scattering in which all the atomic electrons act as scattering centers and the result is a superposition of each contribution. The cross section may be written as

$$\frac{d\sigma_{\text{COH}}(\theta)}{d\Omega} = \frac{d\sigma_{\text{Thomson}}(\theta)}{d\Omega} F(x,Z)^2, \qquad (1)$$

where $F(x,Z)$ is a form factor that is dependent upon the momentum transfer argument, $x[=(1/\lambda)\sin(\theta/2)]$, and the atomic number, Z. This form factor is the Fourier transform of the electron charge distribution of the scatterer; thus, coherent-scatter patterns depend upon the atomic arrangement of the scatterer. This has long been exploited by crystallographers for materials analysis. X-ray crystallography is typically restricted to small, homogeneous specimens, and is, therefore, of limited medical utility. However, these limitations are not fundamental. The size constraint is due to the traditional use of Cu-$K\alpha$ radiation. This monochromatic source ensures a unique relation between scatter angle and momentum transfer, but penetration is limited with a beam energy of only 8 keV. The homogeneity requirement arises because the technique is essentially a projection method of analysis. The use of higher energies and tomographic techniques eliminates these restrictions.

Harding and co-workers first demonstrated that crystallography and medical imaging techniques could be successfully joined to form a powerful new technique, mapping spatial variations in molecular structure throughout an extended,

inhomogeneous specimen.[1,2] Several authors have followed suit[3–13] and proposed various methods for coherent-scatter imaging. Many applications have been proposed for public safety purposes, such as the screening of foodstuffs for contaminants or of checked baggage for explosives or drugs. A commercial system for this purpose has been implemented at Hamburg Airport.[6]

Several medical applications have also been considered. Preliminary studies indicate that coherent-scatter imaging may prove useful in distinguishing benign and malignant tumors from normal breast tissue.[14,15] More recently, the use of coherent scatter to determine the composition of kidney stones has been explored.[16] Treatment for kidney stones is determined in part by their chemical makeup, and, at present, there is no reliable method of determining this *in situ*. Dawson *et al.*[16] used a tungsten anode tube operating at 100 kVp, 1 mAs, and a germanium detector to demonstrate that the coherent-scatter spectra from different stone types could be distinguished one from another.

Perhaps the most exciting application is the characterization of bone based on its coherent-scatter signal.[5,17–19] Bones are comprised of hydroxyapatite (a calcium phosphate salt), collagen, yellow marrow (fat), and bloody marrow (soft tissue).[20] The hydroxyapatite, or bone mineral crystals, are embedded in a collagenous matrix to form bone tissue. This tissue provides bones with rigidity and strength as well as acting as a mineral storehouse for the body as a whole, making bone mineral density (BMD) a useful metric of skeletal health. Metabolic bone diseases form a group of disorders affecting bone tissue, either structurally (osteoporosis) or metabolically (osteomalacia). As osteoporosis progresses, bone tissue is lost and relatively more fat is found in the trabecular space.[21] In osteomalacia, the bone tissue is under-mineralized and soft.[22] For both these diseases, among others, a technique that could provide quantitative maps of the distribution of tissue composition across an axial slice would be useful for investigation as well as diagnosis and monitoring disease and/or treatment progression. It has been shown that the components of bone can be distinguished based on their coherent-scatter patterns[23] and here we present our method for quantitative coherent scatter analysis.

Several factors confound the interpretation of coherent-scatter data from a polyenergetic source as first proposed by Harding.[1] The most fundamental of these is broadening of the scatter patterns due to the energy dependence of the momentum transfer argument. For monoenergetic x rays, the scatter patterns from biological specimens appear as a series of rings of varying brightness. With a polyenergetic source, these rings are smeared out over a range of scatter angles, complicating material identification. Various means of dealing with this have been developed. Harding *et al.* adapted the "white beam" x-ray diffraction method to imaging,[3] using 100 kVp polychromatic radiation and an energy-resolving detector (high-purity germanium) at a fixed angle and performing a raster scan of the specimen. Other groups[8,15] have abandoned diagnostic sources and are developing tomographic systems using high brilliance, monochromatic synchrotron sources. These are not, however, widely accessible. Our approach is to reduce the spectral width of the incident beam with 0.30 g/cm^2 Gd filtration.[4] This reduces the source intensity by 83% but improves the angular resolution of the scatter patterns and allows material discrimination. The scanner is designed so that spectral blurring is minimized while masking other sources of scatter blurring, notably geometrical effects due to finite object and beam size.[4]

In addition to spectral effects, several other influences must be compensated for before accurate quantitative information can be derived from the scatter patterns. First, scatter from sources other than the specimen must be eliminated by careful shielding and design of the primary collimation. Corrections must be made for any nonuniformity in the incident beam intensity as well as for attenuation of the scatter radiation within the specimen itself. As coherent scatter does not have a large cross section for interaction, the signals received by the detection system are low intensity. Detector response must be carefully examined and any nonidealities, such as latency in response times, must be corrected before quantitative information can be extracted from the scatter data. In this article we describe techniques we have developed to rectify each of these effects while producing CSCT images, quickly and with efficient use of the available photons. A quantitative analysis is a necessary precursor to accurate material-specific maps of tissue composition, and here we show that coherent-scatter analysis can provide an accurate measurement of specimen dimensions, material content, and composition in g/cm^3.

II. THE COHERENT-SCATTER CT SCANNER

The CSCT scanner (Fig. 1) is based on a proof-of-concept system previously described by our group.[4] The current arrangement includes refinements to reduce acquisition time, improve scatter detectibility, and facilitate quantitative analysis of CSCT images. The scanner employs a diagnostic x-ray source (Dunlee, Aurora, USA), shielded by 0.5 cm of lead with a 0.5 cm diam hole centered on the focal spot. This prevents any off-focal radiation from interacting with system components and degrading the scatter signal. A second shield is mounted on the back face of the collimator to eliminate photons scattering from the exit hole of the inner shield. Mounted in front of the exit window is a 0.30 g/cm^2 Gd filter. This reduces the root-mean-square (rms) width of the incident spectrum from 27%–14%, improving the angular resolution of the measured cross sections.[4] After filtration, the beam is collimated to an approximately 1 mm^2, square pencil beam using a triple-aperture parallel-plate collimator. This arrangement minimizes scatter from the collimator plates.

The specimen is mounted on a translate–rotate stage and is translated through the beam during a 2–6 s exposure. The transmitted primary is blocked by 5 mm of lead while the coherent scatter from the object is detected by a diagnostic x-ray image intensifier (XRII) (Precise Optics, Bay Shore, USA) coupled to a charge-coupled device (CCD) video camera (Cohu, Poway, USA). Specimen translation and video acquisition are synchronous with an external video signal
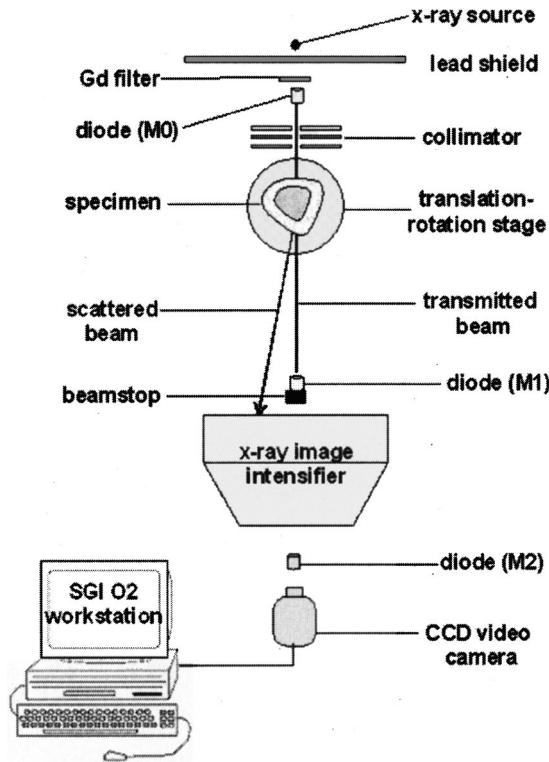
FIG. 1. Schematic of the CSCT scanner.

FIG. 2. Acquisition geometry for CSCT.

generator. Video data is digitized on an SGI-O2 workstation (Silicon Graphics, Inc., Mountain View, USA) such that each video field corresponds to a known specimen position with an accuracy of 0.03 mm. The x-ray intensity is monitored by two detectors, each of which consists of a radiographic screen [Kodak Lanex Fine (Gd$_2$O$_2$S)] optically coupled to a Si photodiode. The first (M0) is mounted on the tube exit window to monitor fluctuations in tube output; the second (M1) is fixed to the primary beam stop. The average intensity of the XRII output phosphor is also monitored by a Si photodiode placed in the parallel beam of the optical path between the XRII and the CCD camera (M2). The signal from each photodiode is digitized at 12 kHz, providing 200 samples per video frame, accurately synchronized to the video clock. The monitor signals are numerically integrated and registered to the appropriate video frame.

III. THEORY

The principle of reconstructing tomographic images from coherent-scatter patterns was first described by Harding et al.[1] and modified by Westmore et al.[5] The theory is briefly summarized here. Figure 2 illustrates the acquisition geometry. The number of photons scattered from an object element of thickness dl, at position l, to the detector element dA is given by

$$dN(\theta) = N_0 T_p(l) n_0(l) \frac{d\sigma_{\text{TOT}}[l,x(\theta,l)]}{d\Omega} \Delta\Omega(\theta,l) T_s(l) dl$$
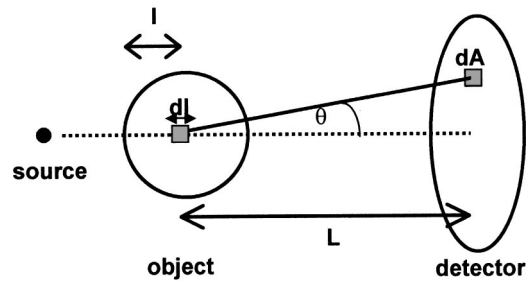$$+ M(l), \qquad (2)$$

where N_0 is the number of incident photons, $T_p(l)$ is the transmission of the primary beam to element dl, $n_0(l)$ is the number density of scattering centers at l, $d\sigma_{\text{TOT}}[l,x(\theta,l)]/d\Omega$ is the total cross section for photon interaction per unit volume per scattering center, $x(\theta,l)$ is the momentum transfer argument, $\Delta\Omega(\theta,l)$ is the solid angle subtended by dA at l, $T_s(l)$ is the transmission of the scatter from dl to dA, and $M(l)$ is the multiple-scatter component. At diagnostic energies, the cross section for coherent scatter is highly forward peaked, while that of Compton scatter falls off sharply as θ decreases.[24] When detection is limited to less than approximately 10°, coherent scatter dominates the differential cross section in Eq. (2).

To obtain an expression that will lead to the reconstruction of tomographic images, Eq. (2) is simplified under a series of assumptions. First, the multiple-scatter component may be neglected if the object size is restricted to less than approximately three half-value layers.[5] In practice, this is achieved by limiting the object size of tissue equivalent materials to less than 10 cm in diameter. Next, the attenuation is assumed to be constant for all scatter paths through the object. Thus, the product $N_0 T_p T_s$ is constant and equal to N_t, defined as the number of photons transmitted through the object. Finally, the l dependence of x and $\Delta\Omega$ can be removed if $L \gg l$ so that the object can be treated as a point scatterer. Thus, $dN(\theta)$ is approximated by

$$dN(\theta) \approx N_t n_0(l) \frac{d\sigma_{\text{COH}}[l,x(\theta)]}{d\Omega} \Delta\Omega(\theta) dl. \qquad (3)$$

Most biological materials are either amorphous or polycrystalline and such materials produce azimuthally symmetric diffraction patterns. It is, therefore, natural to divide the XRII into a series of concentric circular detector elements. Under this geometry, the number of x rays scattered by object element dl into the ith ring is

$$dN_i \approx N_t n_0(l) \frac{d\sigma_{\text{COH}}[l,x(\theta_i)]}{d\Omega} \Delta\Omega_i dl. \qquad (4)$$

Integrating along l gives the total number of x rays scattered into the ith ring:

$$N_i \approx \Delta\Omega_i N_t \int_l n_0(l) \frac{d\sigma_{\text{COH}}[l,x(\theta_i)]}{d\Omega} dl. \qquad (5)$$

Normalizing to unit solid angle and per transmitted x ray gives an expression that is analogous to the line integral of the linear attenuation coefficient in conventional CT:

$$\frac{N_i}{\Delta\Omega_i N_t} \approx \int_l n_0(l) \frac{d\sigma_{\text{COH}}[l, x(\theta_i)]}{d\Omega} dl. \qquad (6)$$

Measuring $N_i / \Delta\Omega_i N_t$ allows for the reconstruction of

$$\gamma[l, x(\theta_i)] = n_0(l) \frac{d\sigma_{\text{COH}}[l, x(\theta_i)]}{d\Omega} \qquad (7)$$

using conventional filtered backprojection. This quantity, $\gamma[l, x(\theta_i)]$, is defined as the differential linear coherent-scatter coefficient per unit solid angle. Unlike conventional CT, where a single image is produced from each projection set, CSCT results in a series of images, indicated by the index i, over a range of scatter angles.

A. XRII temporal lag

The output signal of an XRII is linearly related to the input, but is subject to veiling glare and lag due to decay time constants within the input and output phosphors.[25,26] Scatter patterns are low intensity and XRII glare is assumed to vary in proportion to input intensity at a specific energy. Therefore, by using a lead block to fully attenuate the transmitted primary beam, glare is not expected to be a problem and no attempt has been made to correct for this. The XRII data is captured at a rate of 30 frames per second. Under these conditions, the relatively slow response of the XRII will be misinterpreted as erroneous scatter intensity, resulting in an incorrect density determination.

Temporal lag is described in terms of a temporal impulse response function. To correct for lag, XRII signals are treated as a true lag-free signal convolved with the temporal impulse response function. In principle, the true signal, $T(t)$, could be deconvolved from the measured signal, $M(t)$, using the response function, $R(t)$. In practice, deconvolution can be unstable in the presence of noise and when the impulse response has small values in its Fourier transform. Hence, we developed an approximate convolution correction.

The response of the XRII output signal is assumed linear and temporally shift invariant. Therefore, we can write

$$M(t) = T(t) * R(t). \qquad (8)$$

This allows the calculation of the error due to lag, $E(t)$, as

$$E(t) = T(t) * R(t) - T(t), \qquad (9)$$

and the corrected signal, $M'(t)$, which is approximately equal to the true signal, $T(t)$, is

$$M'(t) = M(t) - E(t) = M(t) - T(t) * R(t) + T(t). \qquad (10)$$

A multiplicative factor, $f(t)$, used to correct for lag is given by

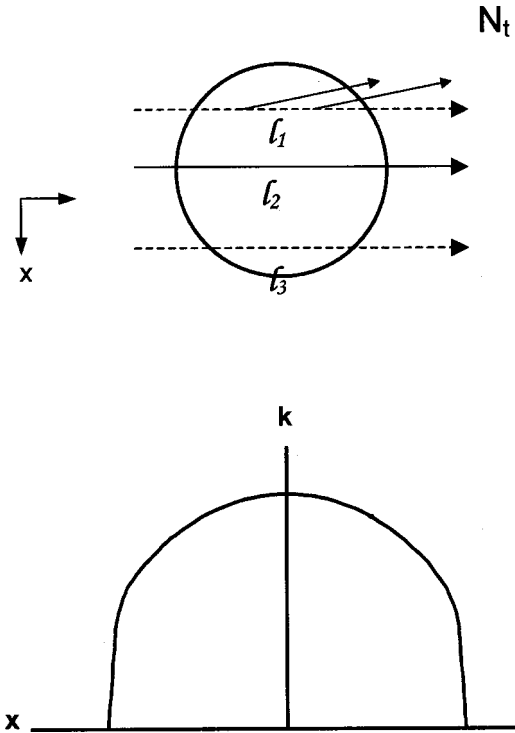$$f(t) = \frac{M'(t)}{M(t)} = 1 + \frac{T(t) - T(t) * R(t)}{M(t)}. \qquad (11)$$

FIG. 3. The self-attenuation problem. For a constant transmission, $N_{tj} = N_t$, over all beam paths, l, through a uniform object, the plot of $k(=1/N_t)$ vs x would be a box. This illustrates that k increases toward the center of the object due to increased attenuation.

It is observed that the error term in Eq. (11) is generally small compared to 1 $[E(t) < 0.1 M(t)]$. It is, therefore acceptable to make the error term in Eq. (11) approximate in that $T(t) \approx M(t)$, giving

$$f(t) \approx 1 + \frac{M(t) - M(t) * R(t)}{M(t)} = 2 - \frac{M(t) * R(t)}{M(t)}. \qquad (12)$$

Thus, the correction factor is determined from the measured signal and $R(t)$, which is determined separately.

The scatter patterns are generally low contrast with little fine spatial detail. We, therefore, make the assumption that the correction factor, $f(t)$, can be applied to an entire scatter-pattern image. Thus, if $I(x, y, t)$ represents a scatter-pattern acquired at time t, the corrected pattern is

$$I'(x, y, t) = I(x, y, t) \cdot f(t). \qquad (13)$$

B. Self-attenuation

The approximations regarding multiple scatter and the l dependence of the momentum transfer argument and solid angle in Eq. (3) are robust with our controlled experimental geometry. The same is not true of the constant-attenuation assumption. Even for a homogenous target, some beam paths will be longer than others, and the attenuation will be larger along those paths (Fig. 3). Using Eq. (6) to reconstruct $\gamma[l, x(\theta_i)]$ results in a cupping artifact. Variations in composition or density will further degrade the images. A straightforward means of correction is to normalize N_i to a measured value of the transmitted primary beam:
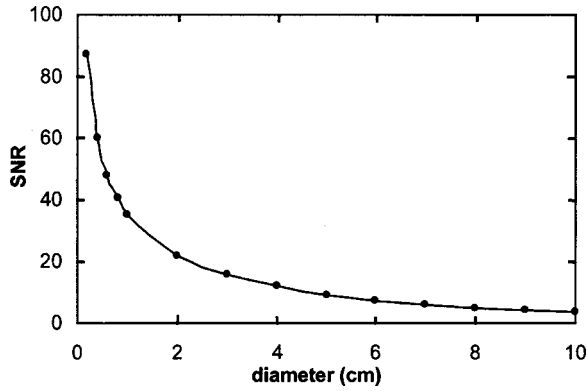
FIG. 4. Variation of peak CSCT image SNR with object size for fixed pixel size and beamwidth.

$$\frac{N_i}{\Delta\Omega_i N_{tj}} = \frac{N_i}{\Delta\Omega_i} k \propto \int_l \gamma[l, x(\theta_i)], \tag{14}$$

where $k = l/N_{tj}$ and N_{tj} is the transmission for the jth ray path. (For each of j rays we obtain a scatter pattern that can be segmented into i annuli.) We are considering only small-angle scatter, therefore the pathlength of the scattered radiation is considered to be equal to that of the transmitted beam. For a deflection of 10°, the scatter pathlength deviates from that of the primary by only 1.5%.

C. CSCT image signal-to-noise ratio

Noise in CSCT images is a potential obstruction to obtaining accurate density measurements. Therefore, it must be ensured that corrections applied to the data do not significantly degrade the signal-to-noise ratio (SNR). It is expected that variations in the measured cross sections will be due to statistical fluctuations in N_i, the number of photons scattered into the ith annulus [Eq. (5)]. N_i is Poisson distributed and the SNR in CSCT images has been shown earlier to be[5]

$$\text{SNR}_i = \left(\frac{12\gamma[x(\theta_i)] m \Delta\Omega_i \Phi_t a^2 b h \epsilon}{\pi^2 W} \right)^{1/2}, \tag{15}$$

where $\gamma[x(\theta_i)]$ is the differential linear coherent-scatter coefficient per unit solid angle at the ith scatter angle for a uniform object, m is the number of projection angles, $\Delta\Omega_i$ is the solid angle subtended by the ith annulus, Φ_t is the incident fluence, a is the pixel size in the reconstructed image, b and h are the height and width of the beam, ϵ is the quantum detection efficiency of the XRII, and W is the object diameter. This result suggests that image SNR decreases with increasing object diameter, and may pose a fundamental limitation for studying larger objects (Fig. 4).

D. Material-specific analysis

Contrast in CSCT images from Eq. (7) depends on both the coherent-scatter cross section of the tissue comprising the specimen and the density of scatterers at each point in the object. The goal of CSCT is to provide volumetric density maps of each tissue component in the form of material-specific images, as described by Westmore *et al.*[5] Cross sec-

tions from pure reference materials, known to be present in the object, are obtained by measuring $N_i/\Delta\Omega_i N_t$ from a single scatter pattern. These are used as a set of basis functions for fitting the experimentally measured $\gamma[l, x(\theta_i)]$ using a non-negative least squares (NNLS) algorithm.[27] The contribution from the kth material, m_k, is determined by minimizing the χ^2 value given by

$$\chi^2 = \sum_i \left(\sum_k \left[m_k \gamma_k[x(\theta_i)] \right] - \gamma[l, x(\theta_i)] \right)^2, \tag{16}$$

where $\gamma_k[x(\theta_i)]$ is the basis function for material k, i is incremented over the series of scatter angles, and k is incremented over the basis materials. This analysis is performed on a pixel-by-pixel basis resulting in a series of images of each component.

Previously published work[5] showed that it is possible to identify materials with this method. However, no attempt was made to quantify the results. In these material-specific images, contrast depends on $n_0(l)$ and the thickness or density of each component material can be calculated according to

$$D_k = m_k D_{k,\text{basis}}, \tag{17}$$

where $D_{k,\text{basis}}$ is the dimension of interest of the basis material and D_k is the quantity desired from the unknown. Obtaining accurate maps of tissue composition requires ensuring that scatter patterns reflect the true magnitude and shape of $\gamma[l, x(\theta_i)]$. Thus, scatter patterns must be corrected for effects such as XRII lag and for self-attenuation of scattered radiation prior to analysis and image formation.

IV. EXPERIMENTAL METHODS

A. XRII Temporal Lag

The temporal impulse response function was determined by exposing the XRII to scatter from a homogenous object for 3 s during a 5 s acquisition. The signal registered by M2 (Fig. 1) is displayed in Fig. 5(a). After demonstrating the temporal response of M2 to be much faster than that of the x-ray rise time using a fast optical LED strobe, the response function, $R(t)$, was determined from the rising portion of the M2 curve [Fig. 5(b)]. The lag correction was tested with simulated data and showed excellent compensation in the absence of noise.[28] The correction factor was determined from Eq. (12), where $M(t)$ was given by the monitor diode, M2, placed in the parallel optical path from the XRII output phosphor. It is, therefore, proportional to the average intensity of the scatter patterns.

B. Self-attenuation

The self-attenuation correction was validated using a 2.5 cm diameter PMMA cylinder. For each of 70 angular views, 70 scatter patterns were acquired as the specimen was translated through the pencil beam during a 2.3 s exposure at 70 kVp and 10 mAs per frame (300 mA). With the Gd filtration, the resulting in-plane average dose delivered to the specimen was 25 mSv. The scatter patterns were corrected for temporal
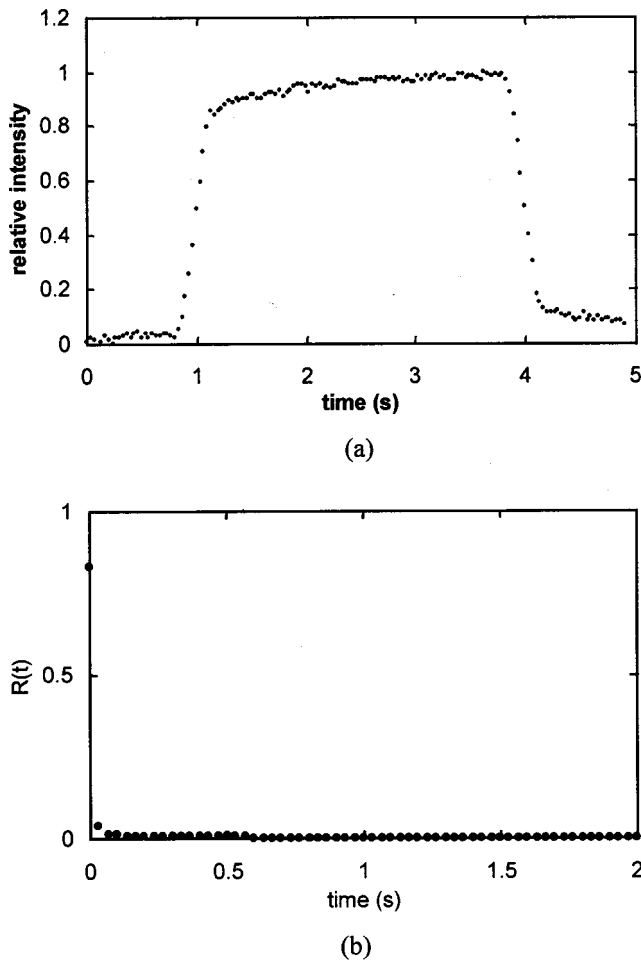
FIG. 5. (a) Measured temporal response of the x-ray image intensifier. The intensifier was exposed to scatter from a homogeneous specimen; excepting fluctuations in photon fluence, the response should be constant during the exposure. The deviation from the ideal case displayed here is due to decay constants in the XRII phosphors. (b) The response function used to correct XRII data for temporal lag, $R(t)$. The response function is not 1 at $t=0$, because $R(t)$ has been normalized to unit area.

lag, and then segmented into concentric annuli representing 100 detector elements. A series of images of the coherent-scatter intensity at 100 scatter angles was reconstructed, first according to Eq. (6) (neglecting self-attenuation), then normalized by the transmitted intensity [Eq. (12)] and reconstructed again to examine the impact of the correction.

C. Noise in CSCT images

Any noise introduced by the lag and self-attenuation corrections was assessed by examining a 10×10 pixel region of interest (ROI) in the center of the PMMA cylinder. For each scatter angle, the mean and standard deviation of this ROI were calculated and the SNR given by the ratio of the two. Experimental SNR values were compared to theoretical expectations using Eq. (15) and values from Table I. The shape of the $\gamma[x(\theta_i)]$ curve was given by the mean values of the ROIs, which were scaled to have the same peak value as given by Kosanetzky et al.[23] The incident spectrum was calculated using the method of Tucker et al.[29] and the entire

TABLE I. Values used to determine the theoretical system signal-to-noise ratio.

m	Φ_t (cm^{-2})	a (cm)	b (cm)	h (cm)	W (cm)	ϵ
70	4.71×10^8	0.05	0.08	0.05	2.5	0.6

spectrum was propagated through the 2.5 cm PMMA object using $\mu(E)$ for the mean beam energy (43 keV) to determine the transmitted fluence. This simplification is within $\sim1\%$ of the more rigorous calculation, which applies the range of $\mu(E)$ values to the spectrum.[5]

D. System linearity

The corrections described above assume a linear system, requiring a linear relative response from each detector (M1, M2, and XRII) with varying input intensities. This was tested by acquiring 5 s of scatter data from a 1 cm block of PMMA at 11 different current settings (25, 32, 50, 63, 80, 100, 125, 160, 200, 250, and 320 mA). The M2 (output phosphor intensity monitor) and video (XRII scatter) data were corrected for lag and attenuation. The diode data was integrated into $\frac{1}{30}$ s bin widths and the total scatter detected by the XRII was integrated.

E. Material-specific images

The original CSCT test phantom was also imaged to demonstrate the impact of system improvements. This phantom mimics the materials of the AAPM low-contrast CT phantom, consisting of a 3.1 cm diam water-filled PMMA cylinder containing 6 mm rods of polyethylene, PMMA, polycarbonate, and nylon (Fig. 6). Scatter-pattern images of each material (basis functions) were acquired at 70 kVp, 1200 mAs then, using the same exposure parameters as for the PMMA cylinder, CSCT and material-specific images were obtained of the test object. The scatter images were corrected
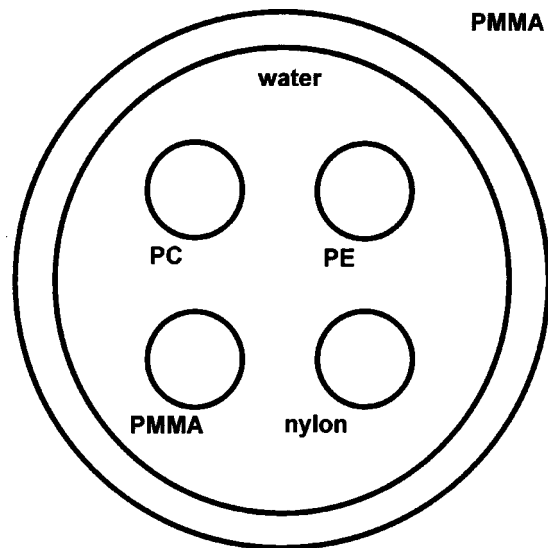

FIG. 6. Schematic of the 3.1 cm diam water-filled phantom containing 6 mm rods of polycarbonate (PC), polyethylene (PE), nylon, and PMMA.
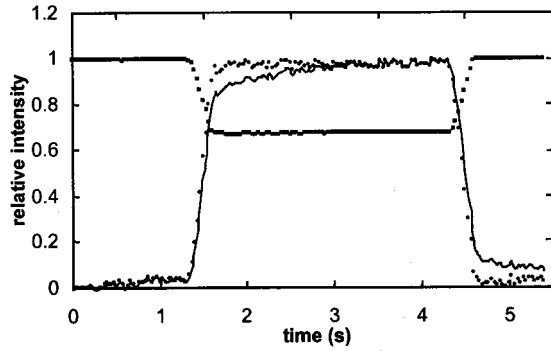
FIG. 7. XRII data for the translation of a piece of PMMA through the x-ray beam, before (—) and after (●) correction for temporal lag. The monitored primary transmission (M1) data is also included (■).

FIG. 9. Noise in CSCT images pre- (▲) and post- (●) attenuation correction.

for XRII lag, integrated in 100 circular detector elements, and normalized to solid angle. The pixel cross sections were then decomposed into linear combinations of the bases using NNLS. This results in independent images of each phantom component.

F. Quantitative materials analysis

Uniform and mixed composition models were used to test the linearity and accuracy of the coherent-scatter analysis method. Data was first acquired from a series of PMMA sheets varying in thickness between 2 and 12 mm in 2 mm increments, as well as from a 5 mm thick sheet. Each sample was exposed for 5.3 s at 70 kVp and 100 mA. The data was corrected for lag and self-attenuation and cross sections were extracted for each sheet. The 5 mm cross section served as a basis function, and the appropriate scaling factors, m_k, relating the basis function to all other cross sections were determined using NNLS. These scaling factors reveal the fraction of the basis function present in each sheet and, thus, determine the thickness of each sheet.

This test was then repeated on a series of five bone-mineral test rods. Each rod contained a different concentration of hydroxyapatite embedded in acrylic (CIRS Inc, Norfolk, USA), ranging from 0 to 0.400 g/cm³ in 0.100 g/cm³ steps. This covers the physiological range of BMD in trabecular bone. Cross sections derived from pure hydroxyapatite and acrylic, of known densities, were used as basis functions
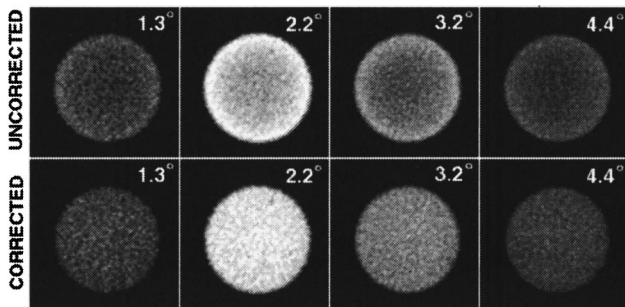

FIG. 8. CSCT images of a 2.5 cm PMMA rod pre- and post-correction for self-attenuation of scatter. The images have a 3.5 cm field of view.
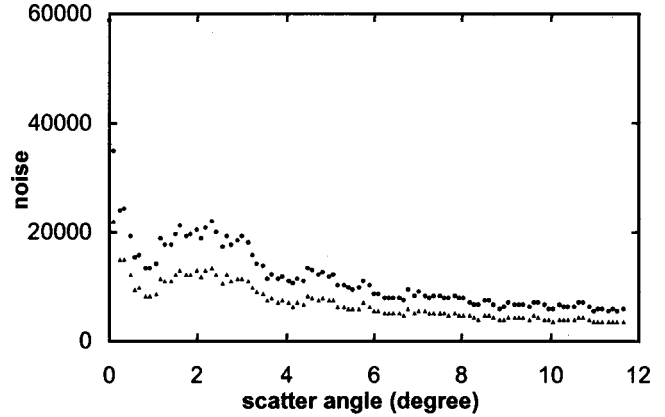
for the NNLS fit. In this case the fit parameters reveal the fraction of the basis density present in each sample.

V. RESULTS

A. Temporal lag in the XRII

The approximate convolution correction was applied to data acquired as a block of PMMA passed through the beam. This case does not result in an instantaneous change in signal. The scatter intensity will grow to full intensity as the object moves fully into the beam. After this, ignoring statistical fluctuations, the scatter signal should be constant across the scan, and then fall to background as the object moves out of the beam. This is illustrated in the transmitted primary curve (M1) in Fig. 7. As this is an attenuation signal, the curve is inverted with respect to the scatter signals.

The XRII data in Fig. 7 clearly exhibits temporal lag. The corrected curve shows considerable improvement. Prior to correction the slope of the "plateau" portion of the curve was 0.042 intensity units/video frame. After correction, this slope is reduced by a factor of 10, to 0.0043 intensity units/ video frame. The residual slope is due in part to components in the XRII temporal response greater than 2 s, which are not corrected for using our approximate method.

B. Self-attenuation

A series of CSCT images of the uniform PMMA rod is displayed in Fig. 8. The uncorrected images (upper row) illustrate the cupping artifact present when self-attenuation of scatter is neglected. Corrected images of the same object (lower row) exhibit the uniform intensity expected from a homogeneous specimen. Visual inspection of Fig. 8 indicates that noise introduced by the attenuation correction does not significantly degrade image quality.

C. Noise in CSCT images

Figure 9 shows the measured noise at each scatter angle before and after all corrections were applied. Although noise levels have increased, the post-correction measured SNR compares favorably to theory, across most scatter angles (Fig. 10). This suggests that the decrease in noise due to
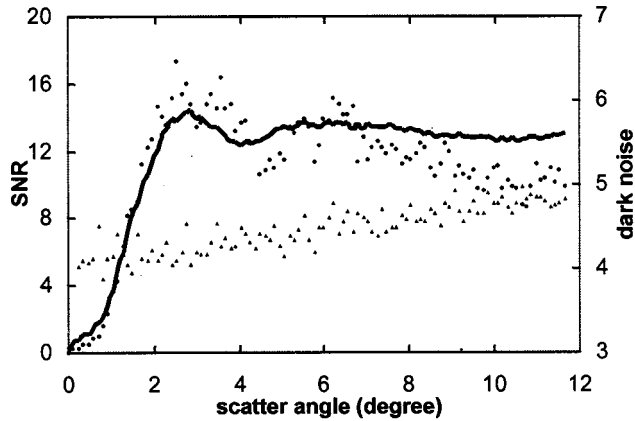
FIG. 10. A comparison of experimentally measured SNR (●), after corrections, with theory (—); also displayed is the standard deviation in the dark level for each ring (▲).

FIG. 11. CSCT images of the low-contrast phantom compared to a simultaneously acquired conventional CT image. The field of view was 3.5 cm.

temporal averaging is correctly restored by this correction method. The deviation between experiment and theory at larger angles is due in part to increased noise contributions from dark subtraction as the area of the integration annulus increases (Fig. 10).

These results must, however, be interpreted with caution. Despite low SNR, CSCT images can display strong contrast between different materials. Material-content information is extracted from these images by using a least-squared analysis of scatter at all angles. Determining the influence of SNR on the material analysis is not straightforward and beyond the scope of this paper. For comparison, the SNR measured in the material-specific image of the 2.5 cm PMMA rod was 18. This is similar to the expected CSCT-image SNR (Figs. 4 and 10).

D. System linearity

The intensity measured by the XRII (scatter), M1 (primary transmission), and M2 (XRII output) were found to be linear with respect to one another. Nonlinearities apparent in the data arise from inconsistencies in the tube output. For each current setting, the three detector results are coincident and the equations for each line are essentially identical, suggesting that each detector is linear with the others. The equation for the intensifier curve is $y = 0.003x - 0.02$, and that of both M1 and M2 is $y = 0.003x - 0.03$, all of which have R^2 values greater than 0.99.

E. Material-specific images

Post-correction CSCT images of the test phantom (Fig. 11) display no trace of self-attenuation artifact at any scatter angle. These images are maps of the coherent-scatter cross-section and, as such, exhibit material-specific, angular-dependent contrast. Material specific results from the water and PMMA components are displayed in Fig. 12. Again, all trace of the self-attenuation artifact has been eliminated.
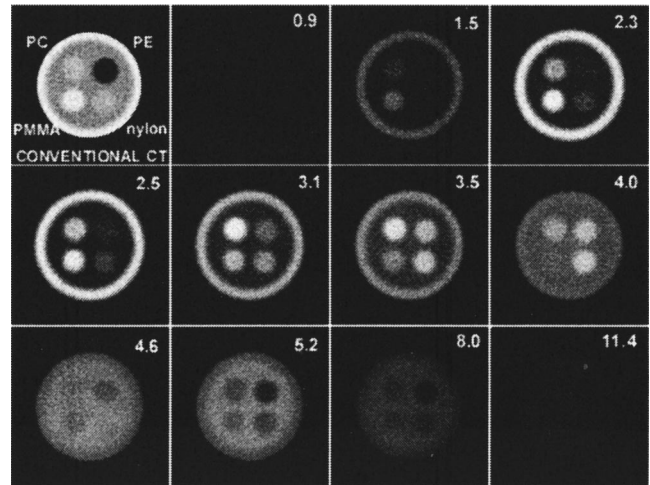
F. Quantitative materials analysis

The first test of the potential quantitative accuracy of the coherent-scatter method involved measuring the thickness of blocks of PMMA. A straight line fit to the data resulted in a line defined by $y = 1.03x - 0.05$, with $R^2 = 0.99$ and an rms error of 0.2 mm.[28] This is in good agreement with the expected straight line through the origin with unity slope.

For the more complicated case of the bone-mineral phantoms, where two materials are combined, material analysis was used to isolate the hydroxyapatite and measure the concentration, [HA], present in each sample. Measured [HA], which simulates a BMD measurement, is plotted versus the concentration reported by the manufacturers in Fig. 13. The straight line fit in this case is given by $y = 1.03x - 0.0002$, with $R^2 = 0.99$ and a rms error of 0.009 g/cm^3. Again, this is in excellent agreement with expectations. While these are simple cases, they do demonstrate that it is possible to make accurate quantifications of material composition and dimension using coherent scatter and illustrates the promise of CSCT as means of analyzing bone disorders.

VI. DISCUSSION

The primary objective of CSCT is to accurately measure the concentration of specific materials at each point in a tomographic slice. This is accomplished by determining the coherent-scatter cross section for each pixel in an image. For the measurements to be accurate, both the structure and magnitude of the measured cross sections must be exact. This paper has outlined several steps required to ensure accuracy.

Image intensifier data is subject to temporal effects due to delays in the phosphor screens, and an approximate correction for this temporal lag has been presented. Estimates of the error in each video frame are determined using a detector with negligible lag to monitor the video output and a single multiplicative correction is applied to each video frame. This correction compensates for lag of no more than 2 s. A significant reduction in the effects of lag were demonstrated (Fig. 7).
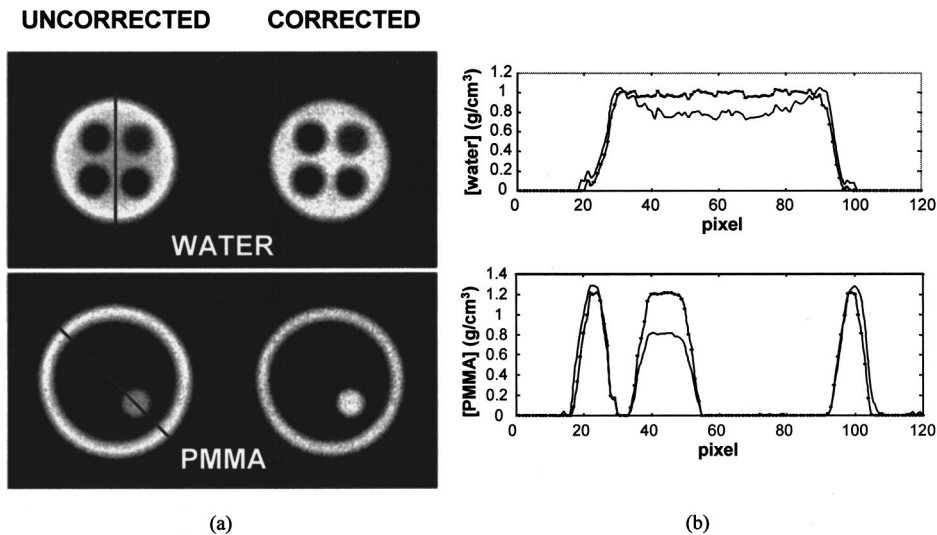
FIG. 12. (a) Material-specific images of the PMMA and water components before and after correction for self-attenuation. (b) Profiles through the material-specific images, at positions indicated in (a), before (---) and after (—) correction.

Preliminary CSCT images suffered from a self-attenuation artifact. This results in intensity cupping in the images (Fig. 8, upper row), which leads to erroneous concentration measurements. Self-attenuation is corrected for by normalizing each scatter projection to the simultaneously measured primary intensity. As Fig. 8 illustrates, this compensates for self-attenuation at all scatter angles. Figures 11 and 12 display a series of CSCT and material-specific images of the CSCT test object. Unlike previously published CSCT images of this object,[5] no cupping is visible in the water and the PMMA rod and cylinder are equally bright at all scatter angles, demonstrating that the correction does not fail in the presence of multiple materials. Again, the material-specific images in Fig. 12 highlight the improvement attained with this correction.

The self-attenuation correction relies on a measure of the transmitted primary beam, which has photon statistics superior to the scattered radiation. Correcting for self-attenuation should not, therefore, degrade the image. This can be confirmed both by visual inspection of Fig. 8 and by the SNR data provided in Fig. 10. Post-correction SNR and theory display excellent agreement.
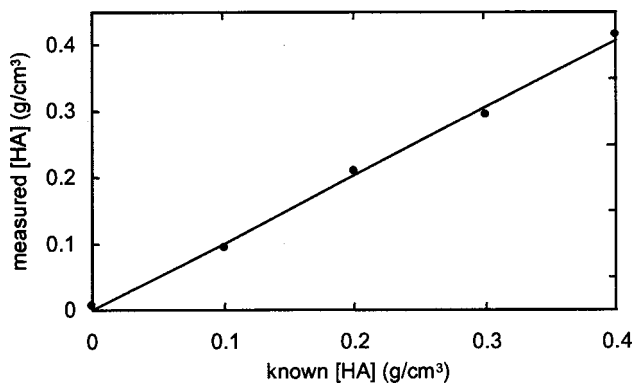

FIG. 13. Hydroxyapatite concentrations ([HA]) measured in acrylic phantoms. The data is compared to the ideal line of unity slope and zero intercept.

Examination of scatter intensity from a 1 cm block of PMMA at a series of increasing tube currents demonstrates the linearity of the system response to variations in intensity. The M2 and video data were corrected for lag before analysis. These results, therefore, indicate not only that the detector chain is linear, but also that the temporal correction is being applied correctly. The quantitative response of the scanner was tested using two simple models in a radiographic mode. For both the simplest case, with only one material present, and the more complex composite case (Fig. 13), the results were very linear. These results demonstrate that we can quantify the thickness or concentration of materials using coherent-scatter-based analysis and also that our system responds linearly to variations in the number of scatterers present in the specimen. These are the first absolute quantifications obtained using CSCT.

VII. CONCLUSIONS

In this paper we describe a method of obtaining quantitative, material-specific information based on x-ray coherent scatter from a specimen. Using an average dose of 25 mSv, PMMA concentrations were measured in a uniform rod with an accuracy of 5%. The results presented here support the development of CSCT for imaging extremities to assess BMD. Current clinical densitometric techniques are susceptible to errors due to variable fat content and tissue density as well as errors due to radiographic matching of calibration materials. CSCT is unaffected by variable composition and uses pure chemical forms of tissue components as basis standards. Thus, CSCT may prove more accurate than other techniques for assessing BMD.

[a] Imaging Research Laboratories, The John P. Robarts Research Institute, P.O. Box 5015, 100 Perth Dr., London, Ontario N6A 5K8, Canada. Telephone: (519) 685-8300 x34130; Fax: (519) 663-3900; electronic mail: icunning@irus.rri.on.ca

[1] G. Harding, J. Kosanetzky, and U. Neitzel, "Elastic scatter computed tomography," Phys. Med. Biol. **30**, 183–186 (1985).

[2] G. Harding, J. Kosanetzky, and U. Neitzel, "X-ray diffraction computed tomography," Med. Phys. **14**, 515–525 (1987).

[3] G. Harding, M. Newton, and J. Kosanetzky, "Energy-dispersive x-ray diffraction tomography," Phys. Med. Biol. **35**, 33–41 (1990).

[4] M. S. Westmore, A. Fenster, and I. A. Cunningham, "Angular-dependent coherent scatter measured with a diagnostic x-ray image intensifier-based imaging system," Med. Phys. **23**, 723–733 (1996).

[5] M. S. Westmore, A. Fenster, and I. A. Cunningham, "Tomographic imaging of the angular-dependent coherent-scatter cross section," Med. Phys. **24**, 3–10 (1997).

[6] G. Harding and B. Schreiber, "Coherent x-ray scatter imaging and its applications in biomedical science and industry," Radiat. Phys. Chem. **56**, 229–245 (1999).

[7] J. A. Grant, M. J. Morgan, J. R. Davis, D. R. Davies, and P. Wells, "X-ray diffraction microtomography," Meas. Sci. Technol. **4**, 83–87 (1993).

[8] J. A. Grant, J. R. Davis, P. Wells, and M. Morgan, "X-ray diffraction tomography at the Australian national beamline facility," Opt. Eng. **33**, 2803–2807 (1994).

[9] J.-P. Schlomka, S. M. Schneider, and G. Harding, "Novel concept for coherent scatter x-ray computed tomography in medical applications," Proc. SPIE **4142**, 218–224 (2000).

[10] S. M. Schneider, J.-P. Schlomka, and G. Harding, "Coherent scatter computed tomography applying a fan-beam geometry," Proc. SPIE **4320**, 754–763 (2001).

[11] R. D. Luggar and W. B. Gilboy, "Recent developments in industrial applications of elastic scatter x-ray inspection," Radiat. Phys. Chem. **56**, 213–227 (1999).

[12] U. Kleuker, P. Suortti, W. Weyrich, and P. Spanne, "Feasibility study of x-ray diffraction computed tomography for medical imaging," Phys. Med. Biol. **43**, 2911–2923 (1998).

[13] G. Martens, H. Bomsdorf, G. Harding, J. Kazenbach, and R. Linde, "Coherent x-ray scatter imaging for foodstuff contamination detection," Proc. SPIE **2092**, 387–398 (1993).

[14] S. H. Evans, D. A. Bradley, D. R. Dance, J. E. Bateman, and C. H. Jones, "Measurement of small-angle photon scattering from some breast tissues and tissue substitute materials," Phys. Med. Biol. **36**, 7–18 (1991).

[15] R. A. Lewis, K. D. Rogers, C. J. Hall, E. Town-Andrews, S. Slawson, A. Evans, S. E. Pinder, I. O. Ellis, C. R. M. Boggis, A. P. Hufton, and D. R. Dance, "Breast cancer diagnosis using scattered x-rays?," Proc. SPIE **4320**, 547–554 (2001).

[16] C. Dawson, J. A. Horrocks, R. Kwong, R. D. Speller, and H. N. Whitfield, "Low-angle x-ray scattering signatures of urinary calculi," World J. Urol. **14**, S43–S47 (1996).

[17] G. L. Royle and R. D. Speller, "Low angle x-ray scattering for bone analysis," Phys. Med. Biol. **36**, 383–389 (1991).

[18] M. Newton, D. L. Hukins, and G. Harding, "Bone composition measured by x-ray scattering," Phys. Med. Biol. **37**, 1339–1347 (1992).

[19] M. J. Farquharson and R. D. Speller, "Trabecular bone mineral density using energy dispersive x-ray diffraction (EDXRD)," Radiat. Phys. Chem. **51**, 4–6 (1998).

[20] R. E. Baron, "Anatomy and ultrastructure of bone," in *Primer on Metabolic Bone Diseases and Disorders of Mineral Metabolism*, edited by M. J. Favus, 3rd ed. (Lippencott-Raven, Philadelphia, 1996), pp. 3–10.

[21] C.-C. Gluer and H. K. Genant, "Impact of marrow fat on accuracy of quantitative CT," J. Comput. Assist. Tomogr. **13**, 1023–1035 (1989).

[22] M. M. Goodsitt, R. F. Kilcoyne, R. A. Gutcheck, M. L. Richardson, and D. I. Rosenthal, "Effect of collagen on bone mineral analysis with CT," Radiology **167**, 787–791 (1988).

[23] J. Kosanetzky, B. Knoerr, G. Harding, and U. Neitzel, "X-ray diffraction measurements of some plastic materials and body tissues," Med. Phys. **14**, 526–532 (1987).

[24] P. C. Johns and M. J. Yaffe, "Coherent scatter in diagnostic radiology," Med. Phys. **10**, 40–50 (1983).

[25] R. K. Swank, "Absorption and noise in x-ray phosphors," J. Appl. Phys. **44**, 4199–4203 (1973).

[26] J. A. Rowlands, "Videofluorography: The role of temporal averaging," Med. Phys. **11**, 129–136 (1984).

[27] C. L. Lawson and R. J. Hanson, *Solving Least Squares Problems* (Prentice–Hall, Englewood Cliffs, NJ, 1974).

[28] D. L. Batchelar, W. Dabrowski, and I. A. Cunningham, "Tomographic imaging of bone composition using coherently scattered x rays," Proc. SPIE **3977**, 353–361 (2000).

[29] D. M. Tucker, G. T. Barnes, and D. P. Chakraborty, "Semiempirical model for generating tungsten target x-ray spectra," Med. Phys. **18**, 211–218 (1991).